AGU ADVANCING EARTH AND SPACE SCIENCES

Geophysical Research Letters

RESEARCH LETTER
10.1029/2025GL118772

Special Collection:
Advanced machine learning in solid earth geoscience

Imaging Hyporheic Exchange by Integrating Deep Learning and Physics-Informed Inversion of Time-Lapse Self-Potential Data

Huichao Yin[1], Scott J. Ikard[2], Dale F. Rucker[3], Scott C. Brooks[4], Zhenxue Dai[5], and Kenneth C. Carroll[1]

[1]Plant & Environmental Sciences Department, New Mexico State University, Las Cruces, NM, USA, [2]U.S. Geological Survey, Oklahoma-Texas Water Science Center, Austin, TX, USA, [3]hydroGEOPHYSICS, Inc., Tucson, AZ, USA, [4]Oak Ridge National Laboratory, Oak Ridge, TN, USA, [5]Institute of Intelligent Simulation and Early Warning for Subsurface Environment, Jilin University, Changchun, China

Abstract Self-potential (SP) monitoring is increasingly used for subsurface flow characterization due to its sensitivity to hydrogeological and geochemical processes. However, SP inversion remains challenging due to its ill-posed nature, sparse data coverage, and strong transient noise. This study proposes a hybrid framework to image hyporheic exchange using a time-lapse SP data set monitored from a streamflow site in Oak Ridge, Tennessee. Dipole moment tomography grids generated from the physics-informed numerical inversion is first used to train a Vision Transformer (ViT) model that maps surface SP sequences to 2D source distributions. While the numerical method is more responsive to transient signals, the ViT model better captures persistent spatial structures. Their complementary outputs are jointly analyzed in the spatiotemporal domain to isolate dynamic hyporheic exchange zones and distinguish transient from steady state subsurface flow features. This approach integrates physical inversion and deep learning to enhance interpretability, generalization, and temporal awareness in SP analysis.

Plain Language Summary Self-potential (SP) signals–naturally occurring voltages measured at the ground surface–can help detect water movement beneath the Earth's surface. However, the inverse problem of turning these surface signals into reliable images of subsurface flow is difficult due to noise and limited data. In this study, we use a combination of physics-based modeling and machine learning to better understand water exchange between a stream and the surrounding ground, known as hyporheic exchange. Using SP data collected over time from a stream site in Oak Ridge, Tennessee, we first apply a physics-informed inversion to estimate flow-related sources underground. These results are then used to train a Vision Transformer (ViT), a type of neural network, to predict subsurface flow patterns from surface measurements. The physics-based model captures immediate changes, while the ViT learns more persistent patterns. Together, they help distinguish between stable and dynamic flow regions, offering new insights into subsurface water behavior.

Key Points:

- Vision Transformer-based inversion of surface self-potential measurement into tomography
- Physically and temporally aware ViT-based inversion model through training on time-lapse self-potential (SP) data set
- Effective subsurface flow pattern identification through integrating numerical- and deep learning-based SP inversion characteristics

Supporting Information:

Supporting Information may be found in the online version of this article.

Correspondence to:

K. C. Carroll,
kccarr@nmsu.edu

Citation:

Yin, H., Ikard, S. J., Rucker, D. F., Brooks, S. C., Dai, Z., & Carroll, K. C. (2025). Imaging hyporheic exchange by integrating deep learning and physics-informed inversion of time-lapse self-potential data. *Geophysical Research Letters*, *52*, e2025GL118772. https://doi.org/10.1029/2025GL118772

Received 12 AUG 2025
Accepted 23 OCT 2025

Author Contributions:

Conceptualization: Huichao Yin, Scott J. Ikard, Zhenxue Dai, Kenneth C. Carroll
Data curation: Huichao Yin, Scott J. Ikard, Dale F. Rucker, Scott C. Brooks, Kenneth C. Carroll
Formal analysis: Huichao Yin, Scott J. Ikard
Funding acquisition: Dale F. Rucker, Scott C. Brooks, Kenneth C. Carroll

1. Introduction

Self-potential (SP) methods provide a passive, noninvasive means to image subsurface flow processes by measuring naturally occurring electric potentials at the Earth's surface (Ikard et al., 2021). These potentials arise primarily from electrokinetic coupling during groundwater movement and are sensitive to fluid fluxes, redox gradients, and permeability contrasts (Han et al., 2022; Mamud, 2023). SP measurements have therefore been applied in hydrology and environmental geophysics to infer seepage pathways, plume migration, or fault-controlled flow (Darnet & Marquis, 2004; Jardani et al., 2006; Revil & Jardani, 2021).

Inverting SP data to recover subsurface source distributions remains a longstanding challenge due to the ill-posed nature of the method and its sensitivity to prior assumptions (Alarouj & Jackson, 2022). Traditional SP inversion approaches, such as nonlinear least squares (Mamud, 2023), typically rely on numerical solvers like finite element methods (Xie et al., 2021, 2023) to solve the Poisson equation (Malovichko et al., 2022), and use optimization algorithms such as Levenberg–Marquardt to stabilize the inversion and recover regularized tomographic source distributions (Mamud, 2023). Solutions may contrast hydrogeological conditions, and strong background noise often impacts their effectiveness on resolving complex source geometries (Rowan et al., 2023). This is especially true for continuously monitored SP measurements where noisy transient signals may be spatially diffused

Investigation: Huichao Yin, Scott J. Ikard, Dale F. Rucker, Scott C. Brooks, Zhenxue Dai
Methodology: Huichao Yin, Kenneth C. Carroll
Project administration: Scott J. Ikard, Dale F. Rucker, Scott C. Brooks, Kenneth C. Carroll
Resources: Scott J. Ikard, Dale F. Rucker, Scott C. Brooks, Kenneth C. Carroll
Software: Huichao Yin
Supervision: Dale F. Rucker, Scott C. Brooks, Kenneth C. Carroll
Validation: Scott J. Ikard
Visualization: Huichao Yin
Writing – original draft: Huichao Yin
Writing – review & editing: Scott J. Ikard, Dale F. Rucker, Scott C. Brooks, Zhenxue Dai, Kenneth C. Carroll

(Alarouj et al., 2021). Over the years, data assimilation has often been necessary to compensate for SP data noise and sparseness, incorporating other data types like electric resistivity (Ikard et al., 2023), hydraulic head (Mamud, 2023), and gravity (Mehanee, 2022). However, data acquisition cost and practicality have become limitations in applications.

Recent advances in machine learning (ML)-based geophysical inversion enable data-driven mapping from SP measurements to subsurface properties. A few types of deep neural networks, including convolutional (Xie et al., 2025), multilayer perceptron (Kaftan et al., 2014), general regression (Durdağ et al., 2022), variational autoencoder (Han et al., 2022), and attention-based architectures (Guo et al., 2024), have been applied in rapid prediction of SP source fields directly from observed data. Despite performance and efficiency advantages exhibited in certain settings enhanced by data assimilation (Yang et al., 2023) and training strategies like few-shot learning (Linjin et al., 2022), most ML-based inversions remain less informed of the governing physics, often leading to limited generalizability, reduced interpretability, and poor sensitivity to transient hydrological responses (Schuster, Chen, & Feng, 2024; Yang et al., 2023).

As a result, the limitations of both numerical and deep learning methods have made it challenging for SP inversion to identify connections between groundwater and surface water. In this study, we propose a subsurface imaging method using continuously recorded SP measurements to establish a hybrid framework of numerical and deep learning-based SP inversion that leverages their complementary strengths. A physics-informed inversion pipeline that integrates particle swarm optimization (PSO) and weighted least squares (WLS) solvers (Ikard, Carroll, Brooks, Rucker, et al., 2024) was used to generate a high-resolution time-lapse SP tomography (Text S1 in Supporting Information S1) data set that was employed for the training of a Vision Transformer (ViT)-based deep learning model to learn how to map surface SP profiles to subsurface source grids. The numerical method enforces physical constraints derived from electrokinetic theory and SP forward modeling with PSO optimization, allowing it to resolve transient flow-induced signals with temporal fidelity. The performance divergence between the numerical and deep learning models was then exploited to take advantage of how responsive the WLS method is to temporally varying SP signals as well as the excellence of the ViT model, trained on the time-lapse data, at capturing persistent structural patterns (Jiang et al., 2025; Raghu et al., 2021; Xiao et al., 2023). By comparing and integrating the outputs of both methods, we aim to isolate regions of dynamic hyporheic exchange and identify steady state versus transient controls on subsurface flow. This framework bridges data-driven generalization with physics-constrained realism, offering a new strategy for interpretable and temporally aware SP inversion.

2. Data Set Description

The data set used in this study was acquired from the floodplain of East Fork Poplar Creek in Oak Ridge, Tennessee, near a site known for its fractured limestone bedrock and active hyporheic exchange (Figure S1 in Supporting Information S1) (Ikard, Carroll, Brooks, Rucker, et al., 2024). Two SP monitoring arrays were installed in March 2023: a line (87 m long with 30 electrodes spaced at 3-m intervals) positioned along the east floodplain, parallel to the stream (offset about 1–3 m from the riverbank) and a perpendicular line (40 m long with 9 electrodes spaced at 5-m intervals) that crosses the fault-feature orthogonally. The perpendicular line intersected the parallel line 40 m downstream from its upstream origin. The monitoring period extended from 26 March 2023, at 16:13 EST to 14 September 2023, at 11:41 EST, during which time electrical-potential differences were measured every 60 s, resulting in a high-resolution, high-frequency data set spanning nearly 226,000-time steps. In addition, an electrical resistivity tomography (ERT) line was collocated with the parallel SP line, to facilitate data validation and integrated analysis (Ikard et al., 2023).

With uninterrupted large-scale temporal coverage, the data set facilitates SP inversions (gridded at 0.5 m resolution to a depth of 10 m) over nearly 6 months, capturing diversified transient groundwater–surface water interactions. In addition, the strategic spatial configuration enables cross-validation and robust model generalization across hydrological settings, with the parallel line placed adjacent to the stream and the perpendicular line intersecting the fault-feature zone for optimal sensitivity to hyporheic fluxes. These characteristics make the data set exceptionally suitable for evaluating inversion algorithms and deep learning models that require representative spatiotemporal inputs, and for advancing hydro-geophysical methods in complex subsurface environments.

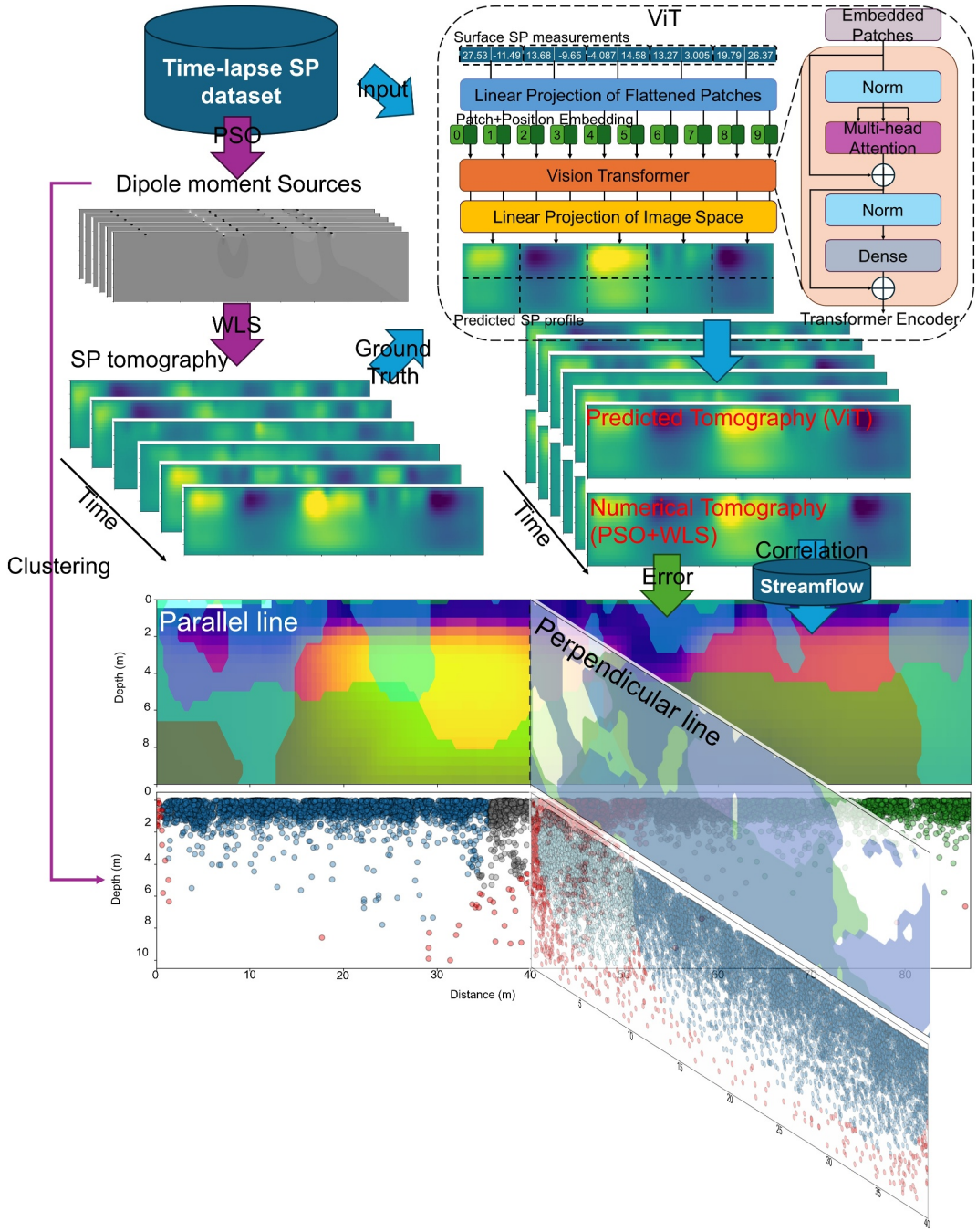

Figure 1. Schematic diagram of the proposed hyporheic exchange imaging framework. The time-lapse self-potential (SP) data set is first inverted using the physical-informed numerical method (particle swarm optimization [PSO] + weighted least squares) to obtain grid-format SP tomography profiles. These profiles serve as ground truth for training a ViT model that learns to predict subsurface dipole moment distributions from surface measurements. Taking advantage of the differing performance capabilities of the deep learning and numerical inversion to evaluate transient SP behaviors, the spatiotemporal prediction errors are subsequently analyzed alongside their correlation with streamflow to investigate hyporheic exchange along the intersected lines of SP measurements. Finally, Dipole moment sources (Text S1 in Supporting Information S1) obtained using PSO are clustered using Density-Based Spatial Clustering of Applications with Noise to validate spatiotemporal source patterns and support interpretation.

3. Methodology

The proposed method is outlined in Figure 1. The time-lapse grid-formatted SP tomography data that were obtained from the monitored data set of surface SP measurements using the numerical method described in Ikard, Carroll, Brooks, Rucker, et al. (2024) and Ikard, Carroll, Brooks, Smith-Vega, et al. (2024) are used as the ViT model ground truth for SP inversion. The PSO-WLS approach for the numerical method combines global and local optimization strategies for robust inversion of SP data. Initially, PSO performs stochastic localization of subsurface dipole sources based on a simplified analytical model defined by Equation 1:

$$\varphi(x) = \sum_{i=1}^{m} p_i \frac{(x - x_0)\cos\theta_i + z_0 \sin\theta_i}{\left[(x - x_0)^2 + z_0^2\right]^{q_i}} \tag{1}$$

which allows for efficient searching of the parameter space without requiring gradient calculations. $\varphi(x)$ (mV) is the electrical potential on any point x along a horizontal profile above an assemblage of electrical-current sources, x_0 (m) and z_0 (m) are, respectively, the origin and depth of the buried electrical source beneath the horizontal profile, θ (radians) is the source's polarization angle, p (mV m^{2q-1}) is the electric-current dipole moment (Text S1 in Supporting Information S1), and q the source's unitless shape factor.

This preconditioning step estimates likely source locations and characteristics. Subsequently, a regularized WLS inversion refines these estimates into a spatially continuous tomographic model by minimizing residuals between observed and simulated SP signals. Incorporating prior information from PSO improves solution stability and convergence, especially under noisy or ill-posed conditions, in order to obtain physically plausible results to train the ViT model with.

3.1. Vision Transformer (ViT) Based Inversion Model

To predict 2D subsurface tomography grids from 1D SP surface measurements, we implement a ViT-based model architecture as shown in Figure 1. ViT operates on sequences of patch embeddings and relies on self-attention to model long-range dependencies (Jiang et al., 2025; Raghu et al., 2021; Xiao et al., 2023), which allow it to capture global patterns in SP tomography frames. Unlike CNNs, which focus on local receptive fields, or LSTMs, which are better suited for temporal sequences, ViT enables efficient global context learning across spatial domains, making it particularly advantageous for detecting diffuse or structurally controlled SP signal patterns. The core mechanism is the scaled dot-product attention, formulated as:

$$\text{Attention}\,(Q, K, V) = \text{softmax}\left(\frac{QK^T}{\sqrt{d_k}}\right)V \tag{2}$$

where Q, K, and V are learned projections of the input, and d_k is the dimension of the key vectors (Harsuko et al., 2025), and softmax denotes the normalized exponential function applied along each row to obtain attention weights. This formulation allows the model to weigh relationships between all SP input positions, making it well-suited for capturing spatial patterns in SP data. The model accepts input SP sequences (of lengths 30 or 9 in this case, which correspond to the number of surface measurement points in the parallel and perpendicular line, respectively) and outputs tomography grids (with dimensions of 20 × 175 and 20 × 81 for the parallel and perpendicular lines, respectively) representing the subsurface dipole moment distribution.

The input SP sequence is split into contiguous, non-overlapping segments called “patches” (Figure 1). For the parallel line, this results in 6 patches of 5 points each; for the perpendicular line, it produces 3 patches of 3 points each. Each patch is then projected into a higher-dimensional feature space through a learnable linear transformation, serving as the input tokens to the Transformer. Learnable positional encodings are added to retain sequential information before the embedded patches are passed through a Transformer encoder comprising 4 layers, each with 4 attention heads and a feedforward dimension of 256. The encoder output is globally averaged along the patch dimension to obtain a fixed-length representation of the input, which is then passed through a two-layer fully connected projection head to regress the flattened tomography grid.

The model enables end-to-end mapping from SP measurements to structured-subsurface representations, capturing non-local dependencies and latent spatial patterns inherent in SP-to-tomography inversion tasks.

3.2. Density-Based Clustering of SP Dipole Moment Sources

To identify spatial groupings of dipole moment sources derived from numerical SP inversion, we employ Density-Based Spatial Clustering of Applications with Noise (DBSCAN). This unsupervised clustering algorithm groups data points based on local point density, without requiring prior knowledge of cluster numbers or shape patterns (Yin et al., 2023), which allows the identification of anomalous dipole sources potentially linked to fracture zones or fluid pathways and supports exploratory analysis in heterogeneous environments.

DBSCAN operates by expanding clusters from core points (those having a minimum number of neighbors within a defined radius ε) and labeling isolated points that do not belong to any dense region as outliers. For this application, clustering is performed on spatial coordinates of the sources, which are filtered for specific polarization angles to isolate vertically aligned dipoles indicative of focused subsurface transport.

4. Results and Discussion

4.1. Self-Potential Data Inversion

For model training and evaluation, the data set is shuffled and split into training, validation, and testing sets with a 7:2:1 ratio, taking advantage of the data set's large sample size. Numerous samples are manually selected to be included in the testing set to facilitate performance evaluation across the entire time domain (including data from the 26th of each month between March and August in addition to 5,000 successive samples starting from the 196,984th min during a rain-driven flood). Additionally, all data samples are standardized to improve model convergence and stability. Mean square error is used as the loss function, whereas structural similarity index (SSIM) and peak signal noise ratio (PSNR) are employed as evaluation metrics (Yin et al., 2024). They are respectively defined as:

$$\mathrm{MSE} = \frac{1}{M \cdot N} \sum_{i=1}^{M} \sum_{j=1}^{N} \left(I_y(i,j) - I_x(i,j)\right)^2 \tag{3}$$

$$\mathrm{SSIM}(x,y) = \frac{\left(2\mu_x\mu_y + c_1\right)\left(2\sigma_{xy} + c_2\right)}{\left(\mu^2{}_x + \mu^2{}_y + c_1\right)\left(\sigma_x{}^2 + \sigma_y{}^2 + c_2\right)} \tag{4}$$

$$\mathrm{PSNR} = 10 \times \log_{10}\left(\frac{\mathrm{MAX}^2}{\mathrm{MSE}}\right) \tag{5}$$

where $I_y\,(i, j)$ and $I_x\,(i, j)$ are grid (i, j) values in the predicted (y) and true (x) SP (inversion) profile (Text S1 in Supporting Information S1), respectively. M and N are, respectively, the profile height and width in grids; μ_x and μ_y, σ_x and σ_y, respectively, denote the luminance mean value and contrast standard deviation of x and y; σ_{xy} is the covariance of profiles; and c_1 and c_2 are stabilizing constants. MAX is the maximum grid value. In addition, root mean squared error (RMSE) is also used in evaluating SP profiles as it penalizes large errors in grids and enhances interpretability by retaining the same data unit. The integration of these metrics is beneficial in investigating grid- and structural-wise measurements on model learning of heterogeneity and a priori information influence on SP measurements and inversions.

In addition, a batch size of 32, Adam optimizer, 10^{-4} learning rate, and an early stopping mechanism with 10-epoch patience are utilized in a training environment implemented by Pytorch in a Windows system on an intel i9-13900K @ 3.00 GHz CPU with 128 GB RAM and a Nvidia RTX 4090 GPU to accelerate computation, resulting in a training time of 41 min. ViT's loss variation over 50 epochs is shown in Figure S2 in Supporting Information S1.

Predicted SP tomography samples on the testing set of the parallel line are shown in Figure 2. All predictions achieved high visual resemblance to their ground truth, with promising RMSE and SSIM values that are respectively less than 0.1 and greater than 0.8, except for rare cases with strong transient SP variations shown in (Figure 2c). The results show that the SP distribution patterns are accurately predicted in ViT results, demonstrating strong variability at depths less than 4 m with consistent horizontal locations to those in true profiles; promising reconstructions of dipole moment grid values are exhibited across both space and time domains. Figure 2g indicates that dipole moment sources localized using PSO from the physics-informed method are

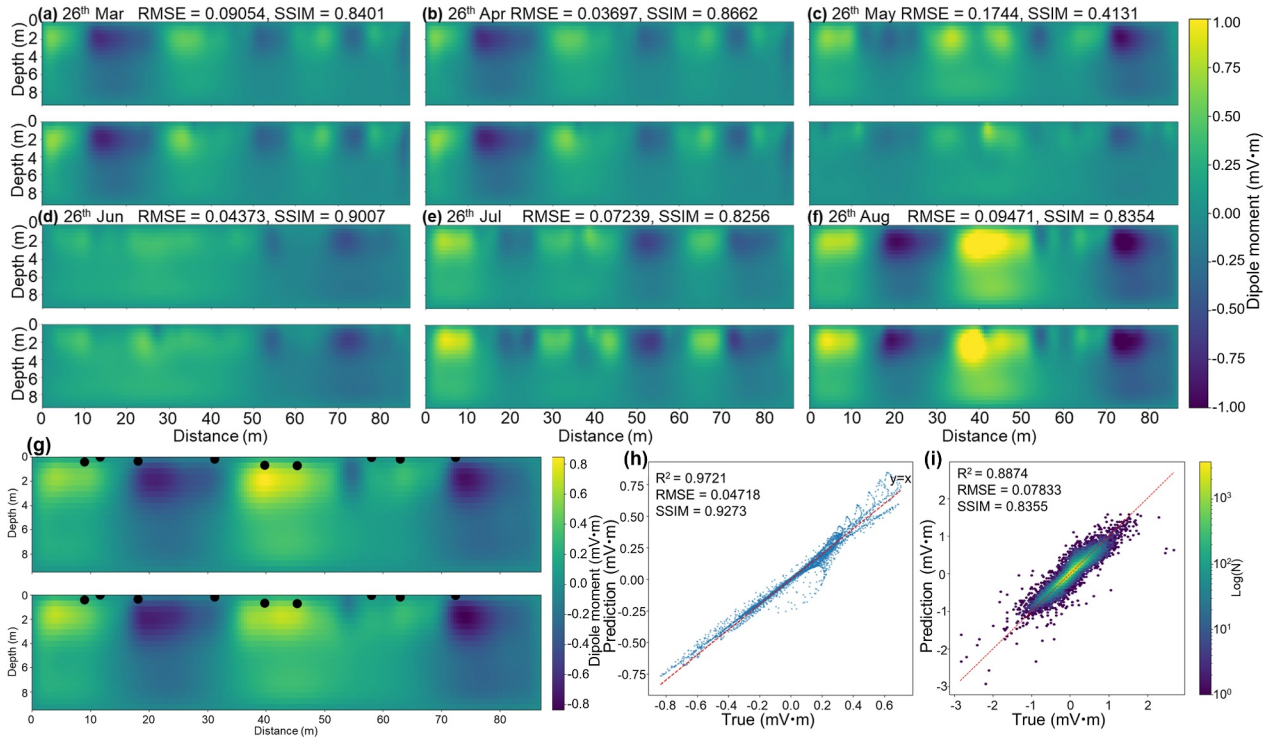

Figure 2. Samples of predicted self-potential (SP) tomography on the parallel line compared to their ground truth on 26th (a) March, (b) April, (c) May, (d) June, (e) July, and (f) August. The top and bottom subplot in each figure are, respectively, predictions from the ViT model and corresponding ground truth. (g) Sample of the dipole moment sources identified by particle swarm optimization (black dots) overlaid on predicted (top) and true (bottom) SP tomography profiles, (h) the predicted over true SP grid values of the sample, and (i) the density plot of the predicted over true SP grid values of 100,000 samples randomly selected across the entire data set.

collocated with areas exhibiting strong SP variability in the predicted profile at shallow depths, demonstrating consistent distribution patterns. This is also reflected in Figure 2h by the close distribution along the identity line as evidenced by the high R^2 value of 0.97. In addition, satisfactory performance is reliably obtained across the entire data set, as indicated in Figure 2i that the scatters are densely distributed along the identity line, resulting in a R^2 value close to 0.89.

The statistics of the model performance metrics over 22,623 samples on the testing set are also satisfactory as shown in Table S1 in Supporting Information S1, demonstrated by the low mean RMSE and high mean SSIM values with low standard deviations. On the other hand, PSNR values are less promising with moderate mean values (less than 30 dB) and higher standard deviations, indicating that the model captures core subsurface SP patterns but may underperform in transient or geologically complex zones, which often leads to a "smooth-out" effect on small-scale or high-frequency SP features as seen in many of the results such as Figures 2c and 2d. Figure S3 in Supporting Information S1 further supports this by showing that RMSE, PSNR, and SSIM exhibit noticeable responses to streamflow and temperature spikes. In Figures S3a–S3c in Supporting Information S1, sharp increases in streamflow frequently preceded elevated RMSE and corresponding drops in PSNR and SSIM, suggesting that short-term hydrologic perturbations momentarily degrade model performance. In Figures S3d–S3f in Supporting Information S1, a similar pattern emerges with respect to stream temperature, where RMSE tends to increase with warming periods while PSNR and SSIM decline, supporting the role of hydrodynamic forcing in affecting model's temporal performance for hydrogeophysical interpretation. On the other hand, during sustained high-flow periods, the metrics stabilize, indicating improved signal coherence, potentially due to increased saturation that suppresses noise. Compared to RMSE and PSNR, SSIM exhibits smaller amplitude fluctuations over time, emphasizing its robustness to transients. This likely arises from SSIM's sensitivity to spatial structure and local contrast, which are less affected under hydrologic transients, especially in regions dominated by persistent geologic controls.

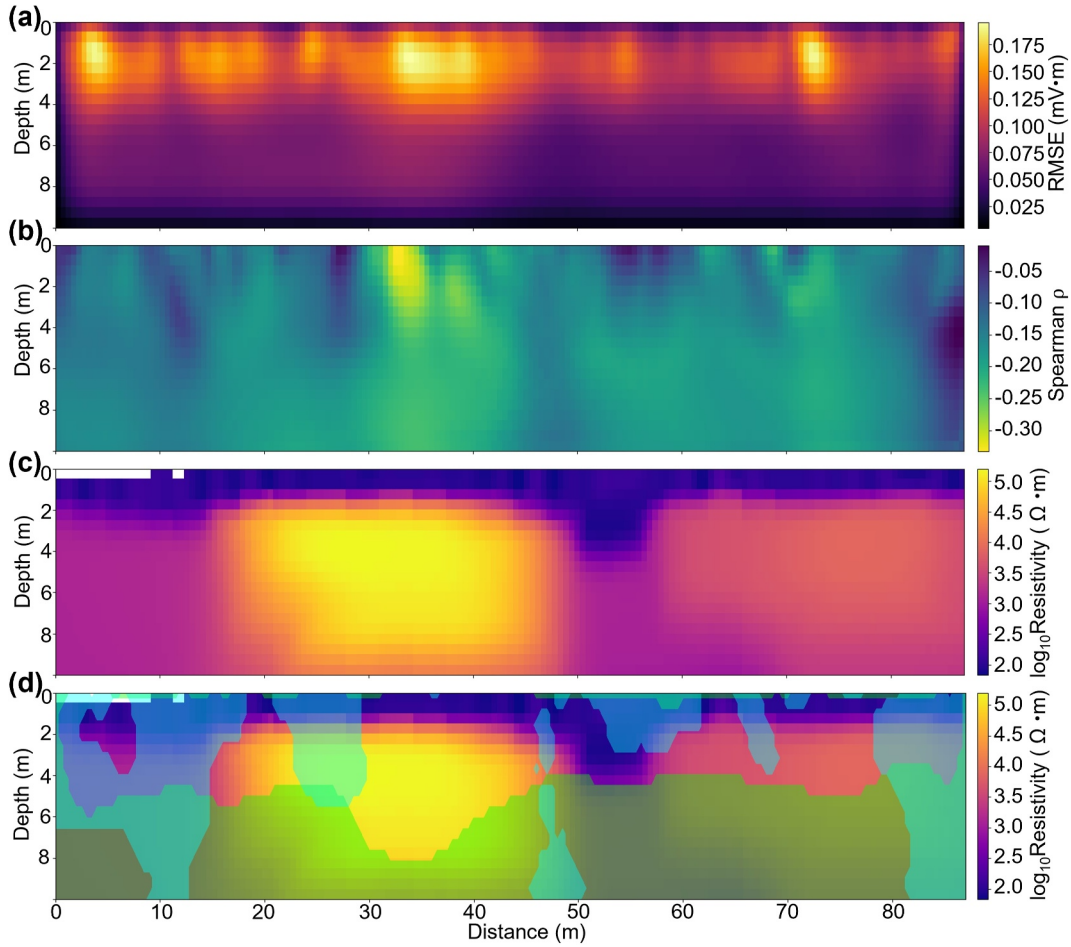

Figure 3. Over the entire observed time domain, calculated grid map of (a) root mean squared error (RMSE) of predicted self-potential tomography, (b) Spearman correlation coefficient between prediction error and streamflow, (c) collocated electrical resistivity tomography (ERT) inversion, and (d) Contour areas of below average RMSE (green) and absolute correlation coefficient (blue) overlaid on the ERT inversion map. The ERT grids have a few missing values on the top left corner due to recording errors. A fault, or karst feature, within the limestone bedrock is inferred to be located between 50 and 60 m within the low-resistivity zone in the ERT profile based on previous studies (Figure S1 in Supporting Information S1) (Ikard, Carroll, Brooks, Rucker, et al., 2024).

To further investigate the model performance characteristics, an animation of the predicted SP tomography was created using 5,000 successive samples starting from the 196,984th min (Movie S1). This time interval coincides with a rain-driven flood hydrograph (Figure S4 in Supporting Information S1). Movie S1 shows clearly that the prediction results' temporal variation is much less active than that of the ground truth, especially at shallow depths, which is undesirable for conducting time-sensitive monitoring of transient subsurface features. However, such features could mask out much of the transient SP response that is mainly caused by surface streamflow while more reliably indicating steady state SP features caused by relatively stationary factors, such as subsurface geological structures. Figure S5 in Supporting Information S1 indicates where the predicted SP profile temporal differentiations are correlated with the streamflow monitored in the observed period, exhibiting distinct spatial patterns that are much more interpretable than those from the ground truth.

4.2. Hyporheic Exchange Imaging

Taking advantage of the differing responses between predicted and ground truth tomography relative to transient SP behavior, we further analyzed the tomography prediction error spatial distribution and its correlations with the monitored streamflow over time to delineate subsurface areas likely to be affected by surface water and the potential connection to groundwater, as shown in Figure 3.

Figures 3a and 3b show that both the prediction error and its correlation with streamflow demonstrate more pronounced variability in shallow areas, and the RMSE remarkably decreases below about 4 m. This is an indication of increased model performance at depth, likely due to reduced surface water influence on transient subsurface SP behavior as depth increases. We note that this contrast with the general expectation in geophysics that uncertainty increases with depth due to signal attenuation and reduced resolution. However, in this case, strong, transient SP signals from near-surface limestone karst features, fractures, or preferential flow paths responding quickly to streamflow via infiltration or recharge, likely cause model underfit and dominate shallow errors. In addition, stratigraphic transitions at bedrock–soil interfaces often contain contrasting electrical properties that lead to complex charge build-up and SP sources. Even though ERT profiles can demonstrate sharp contrast, as shown in Figure 3c, the resulting SP signal may vary continuously or lag.

Furthermore, the correlation map (Figure 3b) presents numerous vertical strips where the absolute values of the correlation coefficient are lower than average. Contours of below average error (blue) and correlation (green) values are overlain on the ERT profile in Figure 3d and demonstrate consistency over their spatial distributions and with ERT patterns, as vertical connections seem to occur between the green and blue contoured areas along matching distance intervals near low resistivity areas, outlining areas where SP behaviors are less correlated with streamflow. The more static model performance in these areas could imply that they are more likely to be under the influence of saturated zones or constant conduits caused by faults, fractures, or karst, which decouple SP from short-term streamflow or temperature variations, suggesting potential groundwater and surface water connections due to hyporheic exchange.

4.3. Result Generalization and Validation

The SP line perpendicular to the streamflow was analyzed with identical procedures. The ViT model was also trained on the perpendicular line data with identical configurations to examine its generalization capabilities (Figure S6, Table S2, and Text S2 in Supporting Information S1). The results on both lines were combined and shown on Figures 4a–4f. The perpendicular line's SP tomography prediction error and its correlation with streamflow were also analyzed as shown in Figure 4g. In addition, PSO-resolved dipole moment sources were spatially clustered using DBSCAN for comparison as shown in Figure 4h. More vertically aligned sources (greater-than-0.7 absolute cosine value of polarization angle) were used for clustering to reduce artifacts of lateral potential differences unrelated to localized features and give a cleaner interpretation of water migration or recharge through fluid pathways.

Figures 4a–4f shows instances of elevated SP variability near the intersection of the two lines, most clearly in midsummer (Figures 4d and 4f), with weaker correspondence in earlier months (Figures 4a–4c), coinciding with an area of the inferred fault or karst feature. This spatial association suggests that, at least during some periods, higher hydrological activity tied to structural heterogeneity may occur here, potentially indicating a preferred flow path for water exchange between the surface water of the creek and the adjacent saturated porous media underlying the floodplain.

Figure 4g presents contours of both low correlation (blue) and low error (green). At the line intersection, the lower 5 m shows similar contour features between the lines, while the perpendicular line exhibits a more extensive low correlation area from 5 to 30 m (distance), suggesting weakening of streamflow's influence. The low error contoured area is mostly located at depth, which is also consistent with the parallel line. However, close to the intersection, error variability is pronounced-higher from 0 to 5 m distance, and lower from 5 to 15 m distance.

Figure 4h illustrates that outliers (red) distribute from 40 to 50 m on the parallel line with less density but substantially higher vertical spread, which intersects with outliers of similar distribution pattern on the perpendicular line. This aligns with the zone of high variability in prediction error and its correlation with streamflow, indicating localized features caused by surface and groundwater connections. The results in Figures 4g and 4h validate each other and strongly support the presence of active vertical charge movement governed by hydrogeologic transition, as the inversion model generalized better with higher stability away from fault, fracture, karst affected, stream-influenced, or highly heterogeneous zones. While the results are validated across the parallel and perpendicular line, method limitations are acknowledged in Text S3 in Supporting Information S1.

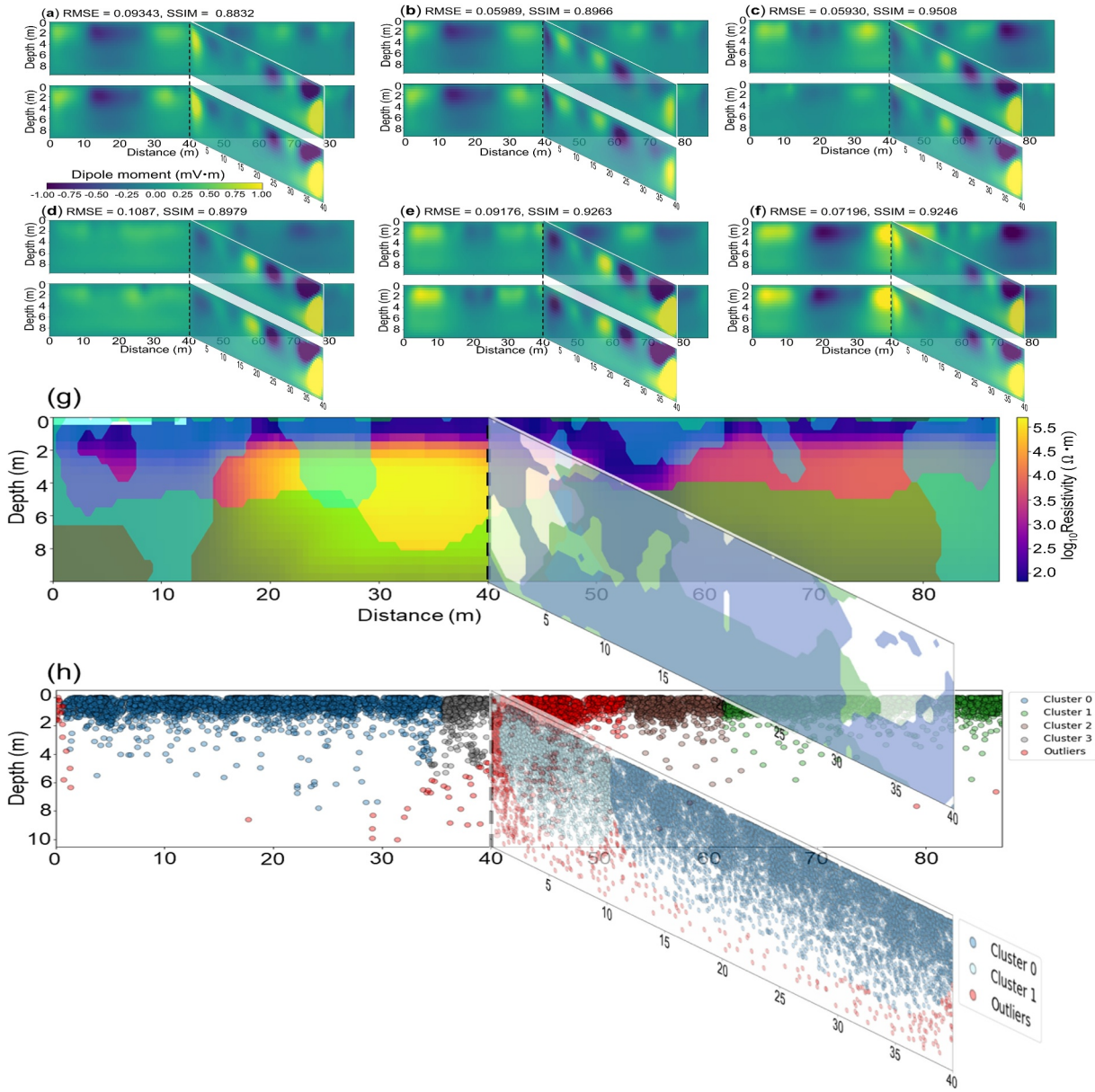

Figure 4. Predicted self-potential (SP) tomography profiles of both parallel (facing toward reader) and perpendicular (facing to the left) lines compared to their ground truth (top and bottom plots, respectively, in each figure). (a–f) Are sampled from March to August, at identical times as Figure 2. The perpendicular results closely resemble ground truth, with root mean squared error (RMSE) and SSIM of about 0.1 and 0.9, respectively. At the line intersection, several months (e.g., panels (d, f)) show visibly similar SP tomography patterns between the two lines, whereas earlier months (a–c) display only partial correspondence. (g) Below average RMSE (green) and absolute correlation coefficient (blue) contour on parallel (overlaid on electrical resistivity tomography profile) and perpendicular line. (h) Spatial clustering of dipole moment sources on both lines. Red scatters are unclassifiable outliers due to distribution density differences. Near the intersection, areas of suppressed prediction error and weaker absolute correlation partly overlap with clusters of dipole-moment sources.

5. Conclusions

This study presents a novel hybrid framework integrating physics-informed numerical inversion and deep learning for imaging hyporheic exchange using time-lapse SP data. A time-resolved SP tomography data set generated by a PSO preconditioned WLS inversion method is used to train a ViT model that predicts subsurface dipole moment distributions from surface SP measurements. By combining the temporal sensitivity of the numerical approach with the ViT model spatial feature learning capabilities, the proposed framework enhances spatiotemporal identification and interpretability in SP-based subsurface flow imaging.

The ViT model demonstrates strong generalization performance across parallel and perpendicular SP monitoring lines and achieves high inversion accuracy. Spatiotemporal analysis of prediction errors and their correlation with streamflow variations reveal consistent subsurface structures and water connections. Furthermore, clustering of dipole sources using DBSCAN supports the presence of focused water pathways and zones of dynamic hyporheic exchange. Beyond its methodological contributions, this integrated approach provides a promising solution for characterizing complex groundwater–surface water interactions in heterogeneous environments, with potential applications in water resource management, contaminant transport monitoring, and ecosystem restoration.

Conflict of Interest

The authors declare no conflicts of interest relevant to this study.

Data Availability Statement

Data is made available in USGS ScienceBase (Ikard, Carroll, Brooks, Smith-Vega, et al., 2024) through Ikard, Carroll, Brooks, Rucker, et al. (2024). Method implementation, trained model weight, and analyzing result data are available at Yin et al. (2025a, 2025b).

Acknowledgments

This work was supported by Department of Energy Minority Serving Institution Partnership Program (MSIPP) managed by the Savannah River National Laboratory under BSRA Contract TOA 800002114. Additional support was provided by the U. S. Department of Energy, Office of Science, Biological and Environmental Research - Research and Development Partnership Pilots (DE-SC0023132) and is a product of the Watershed Dynamics and Evolution Science Focus Area at Oak Ridge National Laboratory. Oak Ridge National Laboratory is managed by UT-Battelle, LLC, for the U.S. Department of Energy under Contract DE-AC05-00OR22725. The authors wish to thank Gladisol Smith-Vega, Aubrey Elwes, Yusen Yuan, and Ahsan Jamil. Any use of trade, firm, or product names is for descriptive purposes only and does not imply endorsement by the U.S. Government. Writings prepared by U.S. Government employees as part of their official duties, including this paper, cannot be copyrighted and are in the public domain.

References

Alarouj, M., Ijioma, A., Graham, M. T., MacAllister, D. J., & Jackson, M. D. (2021). Numerical modelling of self-potential in subsurface reservoirs. *Computers & Geosciences*, *146*, 104656. https://doi.org/10.1016/j.cageo.2020.104656

Alarouj, M., & Jackson, M. D. (2022). Numerical modeling of self-potential in heterogeneous reservoirs. *Geophysics*, *87*(3), E103–E120. https://doi.org/10.1190/geo2021-0265.1

Darnet, M., & Marquis, G. (2004). Modelling streaming potential (SP) signals induced by water movement in the vadose zone. *Journal of Hydrology*, *285*(1–4), 114–124. https://doi.org/10.1016/j.jhydrol.2003.08.010

Durdağ, D., Ayhan Durdağ, G., & Pekşen, E. (2022). Inversion of self-potential data using generalized regression neural network. *Acta Geodaetica et Geophysica*, *57*(4), 589–608. https://doi.org/10.1007/s40328-022-00396-2

Guo, Y. J., Cui, Y. A., Chen, H., Xie, J., Zhang, C., & Liu, J. X. (2024). Self-potential inversion based on attention U-net deep learning network. *Journal of Central South University*, *31*(9), 3156–3167. https://doi.org/10.1007/s11771-024-5755-8

Han, Z., Kang, X., Wu, J., & Shi, X. (2022). Characterization of the non-Gaussian hydraulic conductivity field via deep learning-based inversion of hydraulic-head and self-potential data. *Journal of Hydrology*, *610*, 127830. https://doi.org/10.1016/j.jhydrol.2022.127830

Harsuko, R., Cheng, S., & Alkhalifah, T. (2025). Propagating the prior from shallow to deep with a pre-trained velocity-model generative transformer network. *Journal of Geophysical Research: Machine Learning and Computation*, *2*(1), e2024JH000408. https://doi.org/10.1029/2024jh000408

Ikard, S. J., Briggs, M. A., & Lane, J. W. (2021). Investigation of scale-dependent groundwater/surface-water exchange in rivers by gradient self-potential logging—Numerical modeling and field experiments. *Journal of Environmental & Engineering Geophysics*, *26*(2), 83–98. https://doi.org/10.32389/jeeg20-066

Ikard, S. J., Carroll, K. C., Brooks, S. C., Rucker, D. F., Smith-Vega, G., & Elwes, A. (2024). Self-potential tomography preconditioned by particle swarm optimization—Application to monitoring hyporheic exchange in a bedrock river. *Water Resources Research*, *60*(10), e2024WR037549. https://doi.org/10.1029/2024wr037549

Ikard, S. J., Carroll, K. C., Brooks, S. C., Smith-Vega, G., Elwes, A., & Rucker, D. F. (2024). Self-potential tomography preconditioned by particle swarm optimization—Self-potential monitoring and streamflow data acquired March 26–September 14, 2023 at east Fork Poplar Creek near Oak Ridge Tennessee, with forward and inverse modeling computer scripts [Dataset]. *U.S. Geological Survey Data Release*. https://doi.org/10.5066/P9ASZNJR

Ikard, S. J., Carroll, K. C., Rucker, D. F., Adams, R. F., & Brooks, S. C. (2023). Geoelectric characterization of hyporheic exchange flow in the bedrock-lined streambed of East Fork Poplar Creek, Oak Ridge, Tennessee. *Geophysical Research Letters*, *50*(8), e2022GL102616. https://doi.org/10.1029/2022gl102616

Jardani, A., Dupont, J. P., & Revil, A. (2006). Self-potential signals associated with preferential groundwater flow pathways in sinkholes. *Journal of Geophysical Research*, *111*(B9), B09204. https://doi.org/10.1029/2005jb004231

Jiang, Y., Ma, J., Ning, J., Li, J., Wu, H., & Bao, T. (2025). One-fit-all transformer for multimodal geophysical inversion: Method and application. *Journal of Geophysical Research: Machine Learning and Computation*, *2*(1), e2024JH000432. https://doi.org/10.1029/2024jh000432

Kaftan, I., Sındırgı, P., & Akdemir, Ö. (2014). Inversion of self potential anomalies with multilayer perceptron neural networks. *Pure and Applied Geophysics*, *171*(8), 1939–1949. https://doi.org/10.1007/s00024-014-0778-y

Linjin, Y., Changxin, N., Shuoyang, G., & Guobin, L. (2022). Self-potential forward modeling method based on physics-informed neural networks. In *Paper presented at the Proc.SPIE*.

Malovichko, M. S., Tarasov, A. V., Yavich, N. B., & Titov, K. V. (2022). Application of optimal control to inversion of self-potential data: Theory and synthetic examples. *IEEE Transactions on Geoscience and Remote Sensing*, *60*, 1–11. https://doi.org/10.1109/TGRS.2021.3121538

Mamud, M. L. (2023). *Experimental and modeling approaches to groundwater flow and self-potential for estimating aquifer parameters and investigating surface-groundwater interaction*. (Doctoral dissertation). University of Mississippi.

Mehanee, S. A. (2022). Simultaneous joint inversion of gravity and self-potential data measured along profile: Theory, numerical examples, and a case study from mineral exploration with cross validation from electromagnetic data. *IEEE Transactions on Geoscience and Remote Sensing*, *60*, 1–20. https://doi.org/10.1109/tgrs.2021.3071973

Raghu, M., Unterthiner, T., Kornblith, S., Zhang, C., & Dosovitskiy, A. (2021). Do vision transformers see like convolutional neural networks? In *Paper presented at the 35th annual conference on neural information processing systems (NeurIPS), electr network*.

Revil, A., & Jardani, A. (2021). *The self-potential method: Theory and applications in environmental geosciences* (2nd ed.). Springer. https://doi.org/10.1007/978-3-030-79333-3

Rowan, T., Flynn, R., Butler, A., Jackson, M., Hamill, G., & Donohue, S. (2023). Automated vertical self potential gradient logging and analysis for the tracking of Saline intrusion. In *EGU general assembly conference abstracts* (p. EGU-15408). https://doi.org/10.5194/egusphere-egu23-15408

Schuster, G. T., Chen, Y., & Feng, S. (2024). Review of physics-informed machine-learning inversion of geophysical data. *Geophysics*, *89*(6), T337–T356. https://doi.org/10.1190/geo2023-0615.1

Xiao, H., Li, L., Liu, Q., Zhu, X., & Zhang, Q. (2023). Transformers in medical image segmentation: A review. *Biomedical Signal Processing and Control*, *84*, 104791. https://doi.org/10.1016/j.bspc.2023.104791

Xie, J., Cui, Y. A., Fanidi, M., Zhang, L., Guo, Y., Luo, Y., & Liu, J. (2021). Numerical modeling of marine self-potential from a seafloor hydrothermal ore deposit. *Pure and Applied Geophysics*, *178*(5), 1731–1744. https://doi.org/10.1007/s00024-021-02720-3

Xie, J., Cui, Y. A., Guo, R., Chen, H., Guo, Y., & Liu, J. (2025). A deep learning algorithm for locating contaminant plumes from self-potential: A laboratory perspective. *IEEE Transactions on Geoscience and Remote Sensing*, *63*, 1–13. https://doi.org/10.1109/TGRS.2025.3526947

Xie, J., Du, X., Cui, Y. A., Luo, Y., Zhang, L., Guo, Y., & Liu, J. (2023). Numerical modeling for 4-D self-potential resistivity model. *Pure and Applied Geophysics*, *180*(1), 205–213. https://doi.org/10.1007/s00024-022-03208-4

Yang, L. J., Nai, C. X., Liu, G. B., Lai, K. L., Gao, S. Y., & Zheng, K. D. (2023). Locating the source of self-potential using few-shot learning. *Engineering Applications of Artificial Intelligence*, *121*, 106045. https://doi.org/10.1016/j.engappai.2023.106045

Yin, H., Ikard, S. J., Rucker, D. F., Brooks, S. C., Dai, Z., & Carroll, K. C. (2025a). Data and sample results of paper: Imaging hyporheic exchange by integrating deep learning and physics-informed inversion of time-lapse self-potential data [Dataset]. *Figshare*. https://doi.org/10.6084/m9.figshare.29289401

Yin, H., Ikard, S. J., Rucker, D. F., Brooks, S. C., Dai, Z., & Carroll, K. C. (2025b). Method implementation, trained model weight, and analyzing result data of the paper: Imaging hyporheic exchange by integrating deep learning and physics-informed inversion of time-lapse self-potential data [Software]. *Figshare*. https://doi.org/10.6084/m9.figshare.29289155

Yin, H., Zhang, G., Wu, Q., Cui, F., Yan, B., Yin, S., et al. (2024). Unraveling overlying rock fracturing evolvement for mining water inflow channel prediction: A spatiotemporal analysis using ConvLSTM image reconstruction. *IEEE Transactions on Geoscience and Remote Sensing*, *62*, 1–17. https://doi.org/10.1109/tgrs.2024.3452937

Yin, H., Zhang, G. Z., Wu, Q., Yin, S. X., Soltanian, M. R., Thanh, H. V., & Dai, Z. X. (2023). A deep learning-based data-driven approach for predicting mining water inrush from coal seam floor using microseismic monitoring data. *IEEE Transactions on Geoscience and Remote Sensing*, *61*, 1–15. https://doi.org/10.1109/tgrs.2023.3300012